Modeling the GRB 170202A Fireball from Continuous Observations with the Zadko and the Virgin Island Robotic Telescopes

B. Gendre, N. B. Orange, E. Moore, A. Klotz, D. M. Coward, T. Giblin, P. Gokuldass, D. Morris

The Astrophysical Journal, 929:16 (10pp), 2022 April 10 https://doi.org/10.3847/1538-4357/ac561e

Modeling the GRB 170202A Fireball from Continuous Observations with the Zadko and the Virgin Island Robotic Telescopes

B. Gendre[1,2], N. B. Orange[1,3], E. Moore[2], A. Klotz[4], D. M. Coward[2], T. Giblin[5], P. Gokuldass[1,6], and D. Morris[1,6]
[1] Etelman Observatory Research Center, University of the Virgin Islands, St. Thomas 00802, USVI, USA; bruce.gendre@uwa.edu.au
[2] OzGrav-UWA, 35 Stirling Highway, M013, 6009 Crawley, WA, Australia
[3] OrangeWave Innovative Science, LLC, Moncks Corner, SC 29461, USA
[4] IRAP, Université Toulouse III Paul Sabatier, 9, avenue du Colonel Roche, BP 44346, 31028 Toulouse Cedex 4, France
[5] United States Air Force Academy, Colorado Springs, CO 80840, USA
[6] Department of Chemical and Physical Sciences, University of the Virgin Islands, St Thomas 00802, USVI, USA
Received 2021 November 6; revised 2022 February 7; accepted 2022 February 14; published 2022 April 8

Abstract

We present coordinated observations of GRB 170202A carried out by the Zadko and the Virgin Island Robotic Telescopes. The observations started 59 s after the event trigger, and provided nearly continuous coverage for two days, due to the unique locations of these telescopes. We clearly detected an early rise in optical emission, followed by late optical flares. By complementing these data with archival observations, we show that GRB 170202A is well described by the standard fireball model if multiple reverse shocks are taken into account. Its fireball is evidenced as expanding within a constant-density interstellar medium, with most burst parameters being consistent with the usual ranges found in the literature. The electron and magnetic energy parameters (ϵ_e, ϵ_B) are orders of magnitude smaller than the commonly assumed values. We argue that the global fit of the fireball model achieved by our study should be possible for any burst, pending the availability of a sufficiently comprehensive data set. This conclusion emphasizes the crucial importance of coordinated observation campaigns of gamma-ray bursts, such as the one central to this work, to answer outstanding questions about the underlying physics driving these phenomena.

Unified Astronomy Thesaurus concepts: Gamma-ray bursts (629)

1. Introduction

Gamma-ray bursts (GRBs) are bursts of high-energy photons coming from the far edge of the universe (Klebesadel et al. 1973; Metzger et al. 1997). They are usually considered ideal laboratories for studying extreme physics in the universe (see Zhang 2018 for a review). To do so, a standard unified model, the fireball model (Rees & Mészáros 1992; Mészáros & Rees 1997; Panaitescu et al. 1998) has been patiently constructed and validated against numerous observations (see, e.g., Klotz et al. 2009a, 2009b; Vedrenne & Atteia 2009). With this model and a subset of ground- and space-based observations of a GRB event, it is possible to gain access to the surrounding medium of the progenitor, the physical conditions inside the plasma shell producing the event, and the geometrical constraints of the system. A prime example of this is the study of GRB 110205A by Gendre et al. (2012).

Such a straightforward study of GRBs is unfortunately not very common. This stems, in part, from difficulties with the fireball model and the large degrees of freedom to explain the observed features (Gendre et al. 2009). For instance, technically, all forms of a surrounding medium density (from a constant one to a highly chaotic one) can be accommodated by the model (Panaitescu & Kumar 2000). In practice, either a constant interstellar medium (ISM) or wind environment is considered sufficient to represent the full extent of reality (e.g., Yost et al. 2003). These practices introduce inconsistencies between the observed data and the use of ad hoc model adjustments, and leave unexplored questions as to whether or not more complex environments could explain the observations (Kumar & Zhang 2015). The same can be said for any of the free parameters of the fireball model, which must be fully described to investigate key questions relating to the extreme physics of GRBs. For instance, the magnetic equipartition parameter of the fireball model, ϵ_B, quantifies the energy available from magnetic fields. However, more information is needed to fully deduce the complexity and nature of the magnetic field of the fireball itself (see Zhang & Yan 2011, and references within), especially when considering the fact that these fields can be self-generated by the fireball or be present as "primordial" magnetic fields (Zhang et al. 2003).

The standard fireball model parameters are more easily constrained when the peak of the afterglow emission is observed at a given frequency. Observations that capture the early rise in optical emission are therefore key to constraining GRB models, again akin to the study of GRB 110205A by Gendre et al. (2012). In this paper, we carry out a similar in-depth study of GRB 170202A, an event also accompanied by an extended period of rising optical emission.

Our study focuses on results from the Zadko Telescope and the Virgin Islands Robotic Telescope (VIRT) optical observations, presented in Section 2. The data analysis is explained in Section 3, followed by a discussion about the observations in the context of the fireball model in Section 4. In Section 5, we present a broader discussion about the constraints we placed on the fireball model, before concluding. For our analysis, we adopt a standard Λ cold dark matter cosmology model with $H_0 = 70\,\mathrm{km^{-1}\,s\,Mpc^{-1}}$, $\Omega_M = 0.27$, and $\Omega_\Lambda = 0.73$. All errors are quoted at the 90% confidence level, and we use the standard notation for a given parameter P, $P_x = P \times 10^x$ (when no indices are given, a value of $x = 0$ is assumed).

2. Observations

2.1. High-energy Observatories

The Burst Alert Telescope (BAT; Barthelmy et al. 2005) on board the Neil Gehrels Swift Observatory (Gehrels et al. 2004) triggered on GRB 170202A (trigger = 736407) at 18:28:02 UT on 2017 February 2 (Racusin et al. 2017). The duration of the event was T_{90} (15–350 keV) = 46 ± 12 s (Barthelmy et al. 2017). The X-Ray Telescope (XRT) began observing the field 72.5 s after the BAT trigger (D'Avanzo et al. 2017), while the UltraViolet Optical Monitor started its observations 83 s after the BAT trigger (Kuin & Racusin 2017). Both instruments identified a candidate afterglow at coordinates R. A. = 10:10:03.49 and decl. = +05:00:41.8 (Osborne et al. 2017).

Konus-Wind also triggered on this event, and found the prompt spectrum was best fit by a power law with exponential cutoff, with $E_{\rm peak} = 247^{+166}_{-86}$ keV and a fluence $S = (5.9 \pm 1.4) \times 10^{-6}$ erg cm^{-2} in the 20–10,000 keV range (Frederiks et al. 2017).

The redshift of this event was measured using OSIRIS at the 10.4 m Gran Telescopio Canarias telescope at the Roque de los Muchachos Observatory (La Palma, Spain). The observation started 4.91 hr after the burst, and derived a redshift of 3.645 (de Ugarte Postigo et al. 2017). This translates to an isotropic energy of $E_{\rm iso} \sim 1.7 \times 10^{53}$ erg and $E_{p,i} = 1150$ keV, making this burst compatible with the Amati relation (Amati 2006) when taking into account the intrinsic variability of the relation. Assuming a 30% radiative efficiency, this leads to a total energy budget of $E_0 = 5.67 \times 10^{53}$ ergs.

2.2. The Zadko Telescope

The Zadko Telescope (Coward et al. 2010, 2017) is a 1 m f/4 Ritchey–Chretien telescope situated in the state of Western Australia at longitude 115° 42′ 49″ E and latitude 31° 21′ 24″ S. The telescope was fitted at the time of the GRB 170202A observations with an Andor camera with a back-illuminated charge-coupled device (CCD) covering a 27′ × 27′ field of view, and several filters (SLOAN g′, r′, i′, and Clear). The telescope is fully robotized, and it is specialized in transient source astronomy, with two observation modes: a routine mode, following a schedule built every 6 hr; and an alert mode, responding in less than 10 s to any new transient alert, bypassing the schedule and starting unplanned observations.

In both alert and routine modes, all interactions with the telescope are made remotely, via the internet. Observation requests can be scheduled at any time up to 15 minutes before the start of the night for the routine observations, and at any time for the alert system. The scheduling format is simple, using a text file for the routine mode and a VO-Event packet for the alert mode.

Zadko began observations of GRB 170202A 59 s after the BAT trigger, and followed the event for two consecutive nights. The observations have been reported in Klotz et al. (2017a) and Klotz et al. (2017b).

2.3. The Virgin Island Robotic Telescope

The Etelman Observatory is a Research Center of the University of the Virgin Islands (Orange et al. 2021), located at longitude 64° 57′ 24″ W and latitude 18° 21′ 09″ N (Neff et al. 2004). It is home to a Torus, Inc. robotic system named the Virgin Islands Robotic Telescope (Giblin et al. 2004; Morris et al. 2018). The VIRT is a 0.5 m f/10 Cassegrain telescope on an equatorial mount fork. The telescope instrumentation includes a 12-position Finger Lakes Instrumentation (FLI) filter wheel (presently housing standard Johnson–Cousins UBVRI and Clear filters) and an FLI ProLine 4240 CCD camera containing a back-illuminated Marconi 42–40, 2048 × 2048 pixel sensor. The 13.5 micron pixels provide a 20′ × 20′ field of view and spatial sampling of 0.″5 pixel^{-1}. Its full-frame readout time at full resolution is approximately 2 s.

VIRT is fully robotized, and it can be operated both on-site and remotely, through queue-scheduled and direct user orders. Many nights are characterized by rapidly changing weather conditions (frequent, but usually brief, precipitation events lasting less than 30 minutes), and automated weather-related shutdown capabilities remain in development. As such, an on-site observer oversees the VIRT observing program. The supporting infrastructure of VIRT monitors and warns observers of transient events, with options to bypass the queued-scheduled observing to start unplanned observations (Orange et al. 2021). Observations for VIRT can be scheduled through a web interface, and are compiled approximately every 4 hr.

VIRT took exposures of GRB 170202A for two consecutive nights; however, the data from the second night were lost during Hurricanes Irma and Maria, which struck the facility later that year (Gendre et al. 2019). The first night of observations has been reported in Gendre et al. (2017).

Table 1
Photometric Data of GRB 170202A Extracted from GCN Circulars and Used in Our Analysis

Start (s)	End (s)	Filter	mag	2σ	Reference
39	69	Rc	>17.88	···	Saito et al. (2017)
77	107	Rc	17.19	0.12	Saito et al. (2017)
116	146	Rc	16.56	0.09	Saito et al. (2017)
320	350	R	16.53	0.30	Mori et al. (2017)
6150	6450	R	19.16	0.07	Sonbas et al. (2017)
10200	10680	R	19.65	0.15	Guidorzi et al. (2017a)
15480	15480	r	20.10	0.10	Kruehler et al. (2017)
57504	58044	r	21.10	0.08	Im et al. (2017a)
57717	57957	R	21.10	0.15	Guidorzi et al. (2017b)
141470	142010	r	21.8	0.15	Im et al. (2017b)

Note. For each data point, we provide the start and end times, filter, and 90% confidence level. All magnitudes are expressed in the AB system, and have been converted from the GCN where needed. The data have not been corrected for Galactic or host extinction.

2.4. Other Instruments

Several other instruments responded to the Swift alert, and published their results in various Gamma-ray Coordinates Network Circulars (GCNs). We retrieved only those data taken in red bands, with a precise date of observation. We then converted all of the magnitudes expressed in the Vega system to obtain a homogeneous sample of AB magnitudes. These data are presented in Table 1. Note that they have not been corrected for effects of extinction. For GRB 170202A, the Galactic extinction is negligible ($E_{(B-V)} = 0.02$ mag, $A_R = 0.06$ mag; Schlafy & Finkbeiner 2011).

GRB 170202A occurred while the Middle East and Asian regions were at night, and thus most of the earlier observations

Table 2
Journal of the Swift Observations

Segment	Start (s)	End (s)	Comment
0	86	1841	Pileup in PC mode
1	4990	41,730	⋯
2	57,687	59,667	⋯
3	149,492	151,480	⋯
5	207,123	335,071	⋯
6	436,613	449,494	⋯
7	511,279	522,960	⋯
8	574,342	574,774	No detection
9	626,096	632,254	No detection

were reported from Asia. The diameter range of the involved instruments (30 cm–2.2 m), and its mean of about 1 m, provided deep observations. However, given the redshift of this event, they were not deep enough to cover the entire relativistic part of the optical light curve; specifically, observations of the putative jet break in the optical band are missing (see below). The bulk of the observations were done in the clear or red filters, with some points in the infrared. Again, we checked that the data used for our study were homogeneous in terms of observation, i.e., used similar filters, and that each data point was reported absorbed (i.e., raw).

Lastly, radio observations were performed by the Arcminute Microkelvin Imager, but no detection was reported (Mooley et al. 2017). We incorporate the upper limit derived from these observations into our study, as it additionally constrains our data modeling.

3. Data Reduction and Spectral Analysis

3.1. The Swift/XRT Data

We retrieved the Swift XRT data available at the main HEASARC archive, and reprocessed them using the latest versions of Ftools and CALDB (i.e., 6.26.1 and 20190910, respectively) available at the time of processing. The journal of the observations is provided in Table 2.

The XRT started observations 92 s after the trigger in Window Timing (WT) mode. The instrument switched to the Photon Counting (PC) mode 225 s after the trigger. Between that time and 4990 s after the trigger, the PC data suffered from moderate pileup, and we used the standard method of Vaughan et al. (2006) and Romano et al. (2006) to compare the observed point-spread function and the predicted one. We found that removing the inner 12 pixels solved the pileup issue, and for the first observation in PC mode we used an annulus shape to extract the light curve and spectrum. The successive observations were processed using a standard circular region of radius 25″.

In order to reduce the uncertainties, we used only the non-piled-up data for spectral analysis. The spectra were fit with XSPEC using a simple power law absorbed twice by our galaxy and the host galaxy. The WT and PC spectra are consistent with the same spectral parameters. They are listed in Table 3. As seen in these results, an upper limit was obtained for the host extinction that is attributable to the large redshift of GRB 170202A. The overall fit to the spectra was good, with no evidence of extra features (see Figure 1).

We extracted three light curves—a soft band (0.5–2.0 keV), a hard band (2.0–10.0 keV), and a large band (0.3–10.0 keV)—in order to perform a study of the hardness ratio. We did not find any variability within the error bars, indicating that our initial spectral model was valid for the entirety of the observations analyzed. We then converted the count rate light curves into energy (flux density or flux, depending on need) using our spectral model. The resultant data are presented in Figure 2.

The 2–10 keV band fluxes are found to be 2.7×10^{-10} ergs cm^{-2} s^{-1} and 1.6×10^{-11} ergs cm^{-2} s^{-1} for the WT and PC modes, respectively.

Table 3
Spectral Parameters of the X-Ray Afterglow of GRB 170202A

Parameter	Value	Comment
Galactic N_h (cm^{-2})	2.30×10^{20}	Fixed
Redshift	3.645	Fixed
Extragalactic N_h (cm^{-2})	$<1 \times 10^{22}$	⋯
Spectral index β	0.94 ± 0.09	⋯

Note. We only performed a fit on the WT mode (from 92 to 225 s) for better statistics, as the PC mode suffered from pileup issues. We obtained a χ^2_ν value of 0.92 for 82° of freedom.

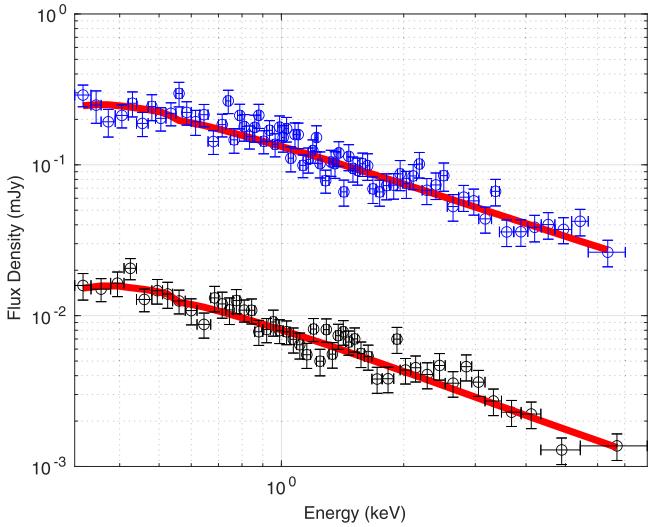

Figure 1. Unfolded X-ray spectrum of GRB 170202A. Top: the WT data. Bottom: the PC data taken during segment number 0 of the observation. The red lines represent the best-fit models. No obvious features are visible in the data.

3.2. The Zadko Data

The Zadko telescope started observations 59 s after the BAT trigger, using the trailing mode observation described in Klotz et al. (2006). Through this technique, stars appear as line segments of constant intensity, and GRB afterglows appear as a line segment with intensity fluctuations that follow its flux variations. Figure 3 presents the trailed image of GRB 170202A from Zadko. Note that its drift length was specifically adopted to cover 30 pixels (40″), with a thickness of 2.″8.

The afterglow of GRB 170202A was located close to a star of 10th mag whose diffuse light overlapped its afterglow trail (see Figure 3). To extract the profile of the afterglow trail, we first subtracted a symmetrical component, with respect to the center of the bright star in the trailed image, to obtain a flat background around it. The resultant profile of the trail was then compared to the profile of a star in the same field. We chose the star 0949-0186220 (NOMAD1; Zacharias et al. 2004) of

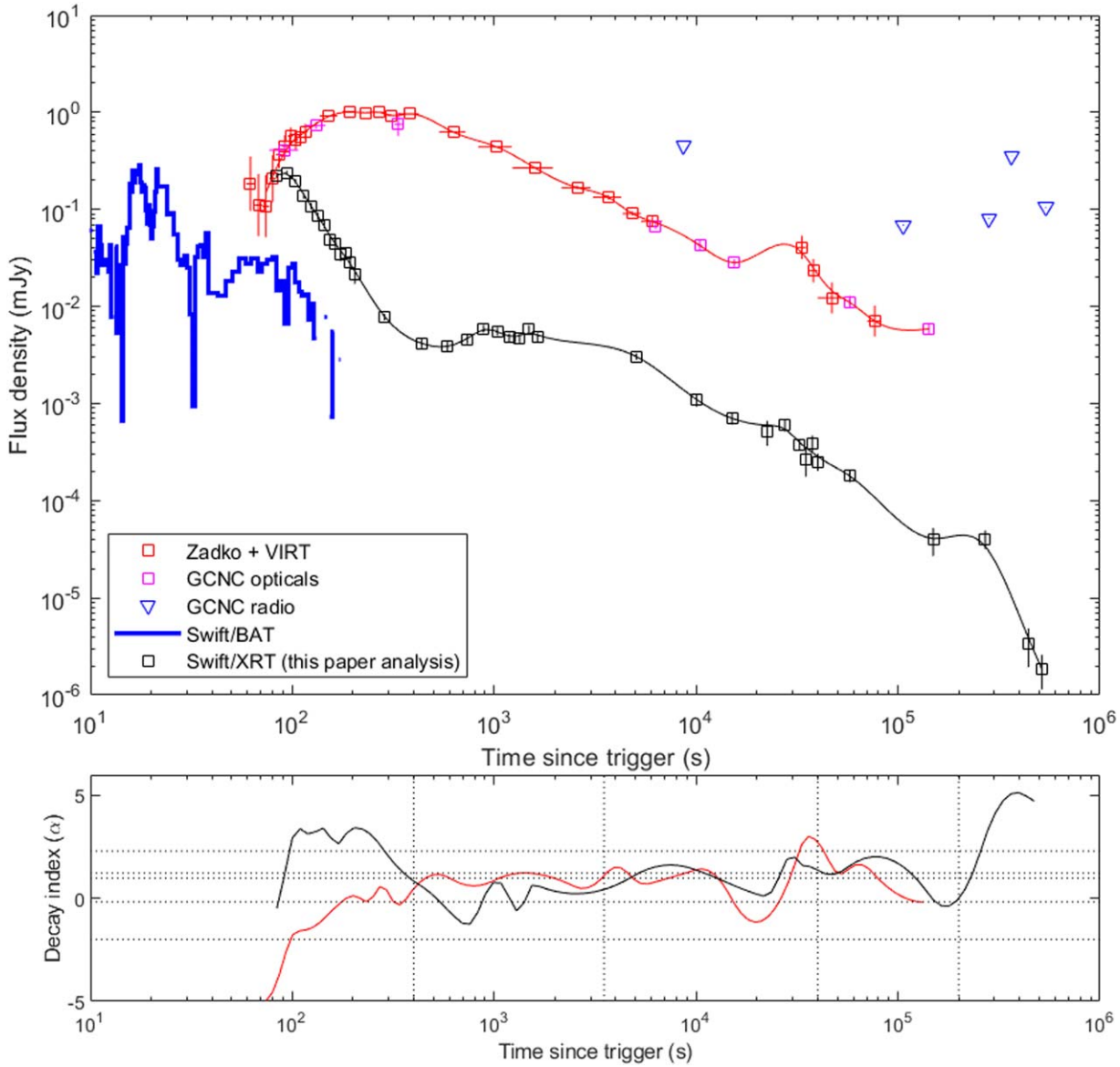

Figure 2. Top: light curves of GRB 170202A in γ, X-ray, optical R, and radio bands. Note that the X-ray light curve is expressed at the 1 keV band and unabsorbed. Bottom: spline fit to the light curve data using a small smoothing factor to detect correlated flares between the various bands. The horizontal dotted lines are the decay indices expected from the various temporal segments of the fireball model (-2, $-1/6$, $(3p-2)/4$, $(3p-3)/4$, and p).

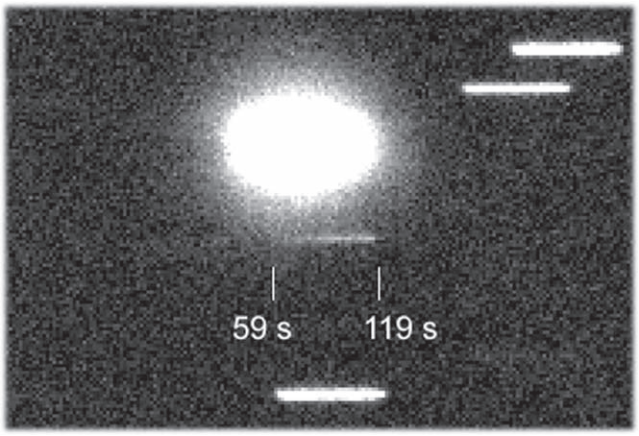

Figure 3. Trailed image of GRB 170202A taken by Zadko. The rising part of its afterglow is clearly observed.

magnitude $R = 14.95$ to convert the GRB afterglow intensity profile into a series of magnitudes. The images obtained after the trailed one were performed with classical sidereal tracking, and coadded to increase the signal-to-noise ratio, for more accurate measures. Like the other optical data, the magnitudes were finally converted into the AB system. These data are listed in Table 4, and presented as red squares in Figure 2.

3.3. The VIRT Data

11 images of 300 s with 1×1 binning were acquired in the clear filter by VIRT, starting from 2017 February 3 at 03:16 UTC. We registered and combined these images to increase the signal-to-noise ratio. The same reference star from the Zadko images was then used to calibrate the flux density of the afterglow (i.e., 0949-0186220, NOMAD1) in the VIRT data, for a more precise correlation between the two instruments. By comparing our reference star to all of the VIRT images, we ensured that the said change in the behavior of the GRB

Table 4
Zadko and VIRT Data

Start (s)	End (s)	R mag	2σ Error	Telescope
59	65	18.06	0.70	Zadko
65	71	18.61	0.80	Zadko
71	77	18.64	0.80	Zadko
77	83	17.93	0.61	Zadko
83	89	17.31	0.35	Zadko
89	95	17.09	0.28	Zadko
95	101	16.83	0.22	Zadko
101	107	16.94	0.25	Zadko
107	113	16.86	0.23	Zadko
113	119	16.72	0.20	Zadko
137	167	16.31	0.01	Zadko
177	207	16.20	0.01	Zadko
216	246	16.23	0.01	Zadko
255	285	16.22	0.01	Zadko
295	325	16.30	0.01	Zadko
334	424	16.26	0.01	Zadko
534	720	16.73	0.01	Zadko
832	1219	17.11	0.01	Zadko
1231	1952	17.65	0.02	Zadko
2152	3000	18.16	0.04	Zadko
3079	4263	18.41	0.06	Zadko
4328	5327	18.83	0.05	Zadko
5338	6777	19.03	0.12	Zadko
31,690	35,093	19.7	0.3	VIRT
36,172	40,003	20.3	0.3	VIRT
40,011	54,065	21.0	0.4	VIRT
70,413	82,773	21.6	0.4	Zadko

Note. The magnitudes are given in the AB system.

afterglow was real, and not due to miscalibration. The importance of this procedure to our work will become clear, as the concatenated light curves of Zadko and VIRT present evidence of intensity variations not expected by the fireball model (see Section 4). The VIRT data are also presented in Figure 2 as red squares.

As indicated in Section 2, a second night of GRB 170202A observations was performed on 2017 February 4 by VIRT. Again, the data were lost during Hurricane Irma, which struck the US Virgin Islands in 2017 September.

4. Fireball Modeling

4.1. Extraction of the Temporal Decays

While the fireball model does not expect spectral features on top of the power-law segments, the situation is very different with actual light curves. There, late internal shocks, refreshed shocks, and fluctuations of the surrounding density can provide significant variability that can complicate temporal analysis. The lower panel of Figure 2 presents the multispectral light curves and decay indices obtained using a spline fit to our data for GRB 170202A. The high degree of fluctuation in the decay indices is a result of keeping the smoothness parameter low to allow the fit to match the maximum number of data points. This easily facilitates the detection of any correlated fluctuation between the optical and X-ray, and indicates deviations from the standard model that can be filtered out.

We define a flare as an episode of rising flux followed by a steep decay seen in optical and/or X-ray. Those not compatible within 3σ of a simple power law from the light curves are removed, and a final fit is performed using only the power-law segments expected by the standard model.

Table 5
List of Temporal Indices (α) of the Light Curves in Figure 2

Band	Segment	Start (s)	End (s)	α
X-ray	Steep decay	⋯	400	3.1 ± 0.2
	Plateau phase	400	5000	-0.2 ± 0.1
	Normal decay	5000	270,000	1.1 ± 0.1
	Late decay	270,000	⋯	2.3 ± 0.3
Optical	Rising part	⋯	150	-3 ± 1
	Slow rising	150	400	-0.2 ± 0.2
	X-ray plateau	400	5000	0.9 ± 0.2
	Normal decay	5000	⋯	0.8 ± 0.2

Note. Note that we use the standard convention $F \propto t^{-\alpha}$, so a negative α indicates an increase of the light curve.

There is a small X-ray flare at ∼20 ks post-burst. The optical data around this time confirm its optical presence. A second, but poorly sampled, flare could also be present in X-ray at ∼190 ks. Our optical data does not cover this epoch. Its last data points, however, present an inflection in the decay indices, which could be suggestive of an achromatic flare (see Figure 2).

Optical flares in GRB afterglows have been studied by Lazzati et al. (2002), who demonstrated that they do not interfere with the global dynamics of the fireball. We therefore ignore them to study the global evolution of the fireball parameters, but do discuss them later, after describing the underlying global emission.

We point out that no obvious change of behavior was witnessed in the optical light curve during and after the X-ray plateau (Figure 2), and that it would have been possible to group the optical phases "X-ray plateau" and "normal decay" (see Table 5) for the analysis into a single phase. Nonetheless, we choose to split the analysis by taking into account the two phases observed in X-ray.

With the above filtering completed, we extract decay indices for multiple segments in the X-ray and optical light curves. Table 5 summarizes these results, along with the temporal definitions we define for each segment.

4.2. The Steep Decay and the Duration of the Event

According to Zhang et al. (2006), the initial part of the X-ray light curve in most GRBs relates to the prompt phase. In this model, the initial steep decay observed in X-ray is the high-latitude emission of the prompt phase, i.e., a delayed flux of photons from the end of the prompt phase (Kumar & Panaitescu 2000). This led Stratta et al. (2013) to define T_X, the temporal break at the start of the steep decay, as the true end time of the emission from the central engine, and the best estimate possible for the duration of the phenomenon.

Following Kumar & Panaitescu (2000), we should have a closure relation between the spectral and decay indices during the steep decay phase, with $C_1 = \alpha - \beta = 2$. As noted in Tables 3 and 5, we measure $\alpha = 3.1 \pm 0.2$ for the steep decay phase of the X-ray light curve and $\beta = 0.94 \pm 0.09$ for its spectral index. This leads to $C_1 = 2.2 \pm 0.3$. The closure relation is thereby valid, and we deduce $T_X \leqslant 100$ s.

Before 100 s, the optical data hint at a small flare. We recognize that the large errors and lack of sampling

accompanying these data at early times make it difficult to validate this event. It is only mentioned here because this kind of flaring activity has been seen since the beginning of GRB observations (Akerlof et al. 2000), with a short duration that does not influence subsequent emission.

One might question why the optical rising index is so poorly constrained, when comparing to the X-ray emission. This is because the fit is dependent on the smoothness of the peak within our model.

After 100 s, the prompt emission of GRB 170202A has ceased. Therefore, the large rise seen in the optical data between ∼80 and ∼200 s should not be linked with the prompt phase, but rather with one of the two remaining components of the fireball: the forward shock and the reverse shock.

4.3. Plateau Phase and Reverse Shock

The Willingale et al. (2007) two-component model of X-ray afterglows attributes the plateau phase as the afterglow onset. Coherently, the start time of the X-ray plateau phase is indeed coincident with the start of the decay of the optical afterglow (Figure 2). However, prior to the X-ray plateau, the optical brightness increases with $\alpha = -3$ (see Table 5). The steepest rise expected from the afterglow model is -2 (Panaitescu & Kumar 2000), which is barely compatible with our observed value. If we consider that the faintest optical data point is due only to the afterglow, and we assume its maximal rise rate from Table 5, then all data earlier than 225 s are located above the theoretical expectation. This indicates an excess of emission over that time. On the other hand, if we assume the slowest possible rise, an excess of emission exists until 2160 s. As a consequence, we assume that the data prior to 225 s are due to a reverse shock, and that the data located between 225 and 2160 s possibly relate to this phenomena. It is difficult to be more precise. Usually, the reverse shock emission should not smoothly merge into the forward shock emission, but rather appear as a break within the light curve (Zhang 2018). We can note (at around 330 s) a small dip into the light curve, which could be interpreted as the end of the reverse shock occurring a little earlier than the peak of the forward shock. However, this dip being so poorly significant (about 2σ), we avoid speculating further about the real date of the end of the reverse shock.

4.4. Electron Distribution Parameter and Surrounding Medium Density Law within the Forward Shock

Using the late afterglow behavior of GRB 170202A, attributable to a forward shock, we derive the model parameters via the methods of Gendre et al. (2007). We start with the properties of the surrounding medium, and the electron distribution parameter, p.

Using Table 4 of Gendre et al. (2007) and the X-ray spectral and temporal indices of GRB 170202A, we can assert that the fireball is expanding in the slow cooling mode, with a cooling frequency (ν_c) located below the X-ray band (ν_X). The optical decay index, however, is not the same as the X-ray one. Instead, it is compatible with a break of $\Delta\alpha = 0.25$. This indicates that the cooling frequency is located above the optical band ($\nu_{\rm opt}$), and the injection frequency (ν_i) is below this band. Such a configuration, and value of $\Delta\alpha$, implies that the fireball is expanding into an ISM of (more or less) constant density.

The near-constant ISM density case corresponds to the equations of Appendix B in Panaitescu & Kumar (2000), which we use to evaluate p with our spectral and temporal indices. We have four indirect and independent measurements of p: three decay indices (two in X-ray, one in optical) and one spectral index. We obtained $p = 2.3 \pm 0.3$, $p = 2.1 \pm 0.2$, $p = 1.9 \pm 0.2$, and $p = 2.1 \pm 0.3$. Reconstructing from these values the probability distribution value of p, and deriving its 90% confidence interval, we obtained $p = 2.05 \pm 0.05$. This value will be used throughout the remainder of this paper.

The optical data between the afterglow peak and the late flares exhibit no temporal breaks, i.e., an absence of any specific frequency crossing. We turn this into the following condition,

$$\nu_i < \nu_{\rm opt} < \nu_c < \nu_X, \quad (1)$$

for GRB 170202A.

4.5. Spectral Energy Distribution and Position of the Injection Frequency

For a shock propagating within the ISM, the peak of each spectral band relates to the passage of the injection frequency and a constant (unabsorbed) flux. We start with the optical band, whose peak at 400 ± 30 s corresponds to the start of the decay phase of the optical afterglow, as stated previously.

In a pure forward shock model, before this epoch, the decay index should be -0.5, but we observe -0.2 ± 0.2. While this is not in agreement with the standard model, we have already highlighted that a portion of our observed emission likely relates to a reverse shock. This phenomenon may explain the difference in the decay index. Consider the model of GRB 170202A developed so far, where a reverse shock could exist until ∼2000 s post-trigger, with the contributions to the observed emission not bright enough to mask the peak of the afterglow. To compute the position of its injection frequency, we need to have some information about $\epsilon_{e,-1}$ and $\epsilon_{B,-2}$. We can use the fact that at the peak of the emission of the forward shock in optical, by definition we are observing at the injection frequency. In doing so, we have:

$$\nu_i = 2.19 \times 10^{17} \epsilon_{e,-1}^{2} \epsilon_{B,-2}^{1/2} = 4.4 \times 10^{14} \rm Hz. \quad (2)$$

It is now possible to compute the position of the injection frequency at any time, and we do so at the time of the radio observations. This is denoted by the red vertical line in Figure 4. The flux at this time is 974 μJ. Note that this gives the maximum of the spectral energy distribution (SED) at any time. Within Figure 4, we denote this by the lower red horizontal line, which corresponds to a model with no extinction.

The cooling frequency provides another constraint on the SED, as we know its position is above the optical band and below the X-ray band at any time (see Equation (1)). This constraint decays with time, so we use the earliest X-ray and latest optical measurements from the period of normal decay. This X-ray measurement results in

$$\nu_c = 1.45 \times 10^{12} n_0^{-1.02} \epsilon_{e,-1}^{-1.07} \epsilon_{B,-3}^{-0.53} < 2.4 \times 10^{17} \rm Hz. \quad (3)$$

The optical value sets a maximum flux at ν_i of 2.9 mJy. This is denoted in Figure 4 by the upper red horizontal line. As this result was constructed with X-ray data, where the host absorption is negligible, our model corresponds with the maximal amount of extinction due to the host. The final model,

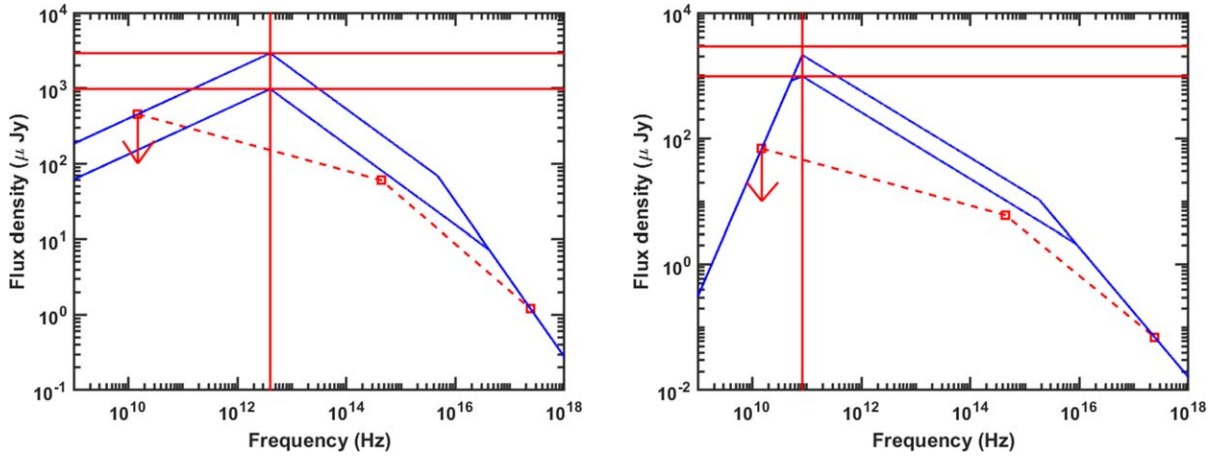

Figure 4. SED of the GRB 170202A fireball at the time of the first (left panel) and second (right panel) radio observations (see Figure 2). We indicate in red the constraints imposed by the model (see the text for the explanations) and in blue its limits.

therefore, must fall between these constraints to fit the global observations, taking into account the real host extinction.

As these constraints evolve with time, we refine them by considering the upper limits for GRB 170202A reported in radio. To do so, the first step is to construct the SED at the time of each radio observation, and then to compute the evolution of the constraints. Figure 4 presents the results, with the radio observation at $t = 8685$ s (left) and the one at $t = 106{,}317$ s (right).

Interestingly, we find that the second radio upper limit, which is deeper than the first one, implies that the self-absorption frequency is located at $\nu_a > 15$ GHz. This does not aid in constraining the first SED, so it is left out of Figure 4 (left panel) for clarity. Our upper radio limit does force a lower limit on ν_a, namely

$$\nu_a = 2.6 \times 10^9 E_{53}^{1/5} n_0^{3/5} \epsilon_{e,-1}^{-1} \epsilon_{B,-2}^{1/5} > 15 \times 10^9 \mathrm{Hz}. \quad (4)$$

4.6. Optical Extinction and Surrounding Density

The value of the surrounding density parameter is usually obtained through radio measurements (e.g., Gendre et al. 2007). However, in the case of GRB 170202A, no radio detection was reported (see Section 2). This required an ad hoc fix. In the right panel of Figure 4, it is seen that the optical data requires an amount of extinction linked to the host galaxy, to match the expected model. We derived a value of A_R between 0.58 and 1.43.

We cannot discern the type of extinction law that should be used (i.e., Milky Way versus Magellanic Cloud laws), but we can better constrain the value of the density parameter. Our 0.58–1.43 range of optical extinction is typical of a normal ISM density. This rules out the cases of either $n_0 \gg 1$ or $n_0 \ll 1$. It is worthwhile to point out that the effect of this parameter on our previous equations scales with a power far less than 1. Therefore, its effects on the outcomes of this study are small, and we safely assume that $n_0 \sim 1$ is a sufficient first-order approximation to the surrounding medium density of GRB 170202A.

4.7. The Microphysics Parameters

Returning to our equations for specific frequencies, we can now derive the microphysics parameters of the GRB 170202A fireball. Specifically, ϵ_e and ϵ_B, which give the fireball energy distribution between electrons and the magnetic field, respectively. Using Equation (2), we obtain

$$\epsilon_e = 1.41 \times 10^{-3} \epsilon_B^{-1/4}, \quad (5)$$

and from equation B8 of Panaitescu & Kumar (2000), the flux observed in X-ray during the second SED leads to

$$F_\nu = 3.40 \times 10^{-4} \epsilon_{e,-1}^{1.05} \epsilon_{B,-2}^{0.01}, \\ = 0.7 \times 10^{-4} \mathrm{mJy}. \quad (6)$$

By combing Equations (5) and (6), we then arrive at

$$\epsilon_e = 0.0216, \\ \epsilon_B = 1.84 \times 10^{-5}. \quad (7)$$

4.8. The Jet and Its Opening Angle

The late break observed in the X-ray light curve could be due to either a jet break or a cooling break (Figure 2). As argued below, the former hypothesis is favored by three tests we can apply to our data.

First, a cooling break would imply a difference on the decay indices of $\Delta\alpha = 0.25$ (Panaitescu & Kumar 2000). This is significantly less than the $\Delta\alpha = 1.2 \pm 0.3$ we found for GRB 170202A. Second, our value of $\Delta\alpha$ would imply an unrealistic value of the electron distribution index of the burst, i.e., $p \sim 3.7$. Lastly, a jet break should be achromatic, while a cooling break should not (Kumar & Panaitescu 2000; Panaitescu & Kumar 2000). We lack the optical data necessary to confirm achromatic behavior at this period in our burst, and its optical limits offer no further constraints to our model. Despite the inconclusive nature of this last test, the first two strongly oppose the null hypothesis. Thus, we consider that the late break of GRB 170202A results from the effects of a relativistic jet.

With the surrounding medium structure determined, we derive the jet aperture angle. For the ISM case, we use the work of Sari et al. (1999) to write

$$\theta = 0.002 E_{52}^{-1/8} t_b^{3/8} n_0^{1/8} = 0.13 n_0^{1/8}, \quad (8)$$

whose result is expressed in radians. In Equation (8), note that t_b is the jet break time in seconds, and the X-ray data of GRB 170202A gives $t_b = 270{,}000$ s (see Table 5). Using these

results, we arrive at $\theta \sim 7.^{\circ}5$, which is typical for GRBs (Frail et al. 2001; Fong et al. 2015).

4.9. The Deceleration Radius

The deceleration radius is reached when the afterglow emission stops brightening in all wavelengths. Because the initial afterglow emission is likely mixed with that of a reverse shock and late prompt emission, a precise time cannot be extracted for its deceleration. Though we can consider that the deceleration of this burst started when the optical emission started to decay, i.e., $t_{\rm dec} < 400 \pm 30$ s (Figure 2 and Table 5). This value constrains the initial Lorentz factor of the fireball, according to the equation

$$\Gamma_{2.47} = 1.15 t_{\rm dec,rest}^{-3/8} E_{52}^{1/8} n_0^{-1/8} > 1.02 n_0^{-1/8}. \quad (9)$$

Plugging in $n_0 = 1$ (as discussed previously), we find $\Gamma > 300$ for GRB 17020A.

4.10. The Flares

We finally focus on the last component of our model, the flares. There are two episodes of flare-like rebrightenings for GRB 170202A (Figure 2). The first is visible both in optical and X-ray, and peaks at about 20 ks post-trigger. A second rebrightening was only visible in X-ray at ∼190 ks, but as we have already pointed out, optical data was not available for this epoch, so further discussions are avoided.

Note that the optical component of the first flaring event is brighter than that of the X-ray. This contradicts the "normal" X-ray flares witnessed in other bursts, i.e., the optical component is dimmer (see Krühler et al. 2009, for one example). From the model we have built so far, this type of flaring event is not possible from either density fluctuations or the injection of energy. In fact, its X-ray flux should be independent of the ambient density, because the X-ray frequency is above the cooling frequency (Kumar 2000). Alternatively, in the case of a late injection of energy, we should expect a correlated and scaled behavior in the X-ray and optical light curves. This is not what has been observed: the optical flare is brighter than the X-ray counterpart.

To explain the GRB 170202A flaring event, we return to the argument of a reverse shock. The X-ray component of this flare is considered to follow the widely accepted idea of an injection of energy from a late internal shock (e.g., Zhang 2018). We then argue that an excess of observed optical emission, compared to its X-ray counterpart, is a combined result of this late internal shock and a reverse shock, which it can easily produce (e.g., see Gao et al. 2013, and our discussion below).

Gao et al. (2015) suggested that the magnetic energy in a reverse shock is roughly 100 times greater than that of the forward shock. For GRB 170202A, the late mixing of the forward shock, refreshed energy injection, and flaring with contributions from a late reverse shock make it impossible to disentangle the energetic details of such a reverse shock. With that said, the value ϵ_B within the reverse shock cannot be quantified, but a value of $\sim 100 \times \epsilon_B$ (of the forward shock), i.e., 2×10^{-3}, would reasonably explain the optical excesses observed for the late GRB 170202A flare.

5. Discussion and Conclusion

Table 6 summarizes our model of GRB 170202A. The bulk of it was constrained by observations, with the exception of the surrounding medium density and the position of the peak of the afterglow emission. We assumed that the peak of the afterglow corresponded to the last observed optical point before the onset of a decay in its light curve. While this assertion does influence the value of Γ, it has no effect on ϵ_e and ϵ_B. For comparison, consider the values of ϵ_e and ϵ_B that were derived similarly for GRB 110205A, e.g., see Table 6 and Gendre et al. (2012).

The Lorentz factor of GRB 170202A is far greater than that of GRB 110205A. GRB 110205A was known to be a "slow" event, in that it allowed each component of the fireball to be observed one after the other. GRB 170202A seems to be a more common burst, where all the fireball components are observed more or less simultaneously. Given the compliance of GRB 170202A with the Amati relation (see Section 2), we consider that the fireball parameters of this burst are representative of a typical GRB.

The ϵ_e and ϵ_B results for GRB 170202A are far smaller than those expected by the standard fireball model, i.e., the $\epsilon_e \sim 0.1$ and $\epsilon_B \sim 0.01$ of Panaitescu & Kumar (2000). Our results, however, are in agreement with the work of Gao et al. (2015), who reported a similar partition between the electron and magnetic field energy using Monte Carlo simulations. We also point out that the ϵ_B reported for GRB 110205A is far larger than that found for GRB 170202A, while the opposite can be said of their initial Lorentz factors (see Table 6). This observation is interesting, as it may suggest that a link exists between the initial Lorentz factor and the magnetic energy of the fireball.

The complexity from mixing afterglow components could have been misconstrued at the onset of this study as an inability to model the fireball of GRB 170202A sufficiently. We have shown that such is not the case, and that, pending the availability of a comprehensive enough data set, it is feasible to extract the relevant physics. Unfortunately, the reverse shock parameters are not well constrained for GRB 170202A. Such could be obtained for future bursts, if the temporal coverage were to be more dense than that available to this study. This emphasizes the importance of and need for a global network of telescopes providing continuous observations of GRBs for several days.

Our study has exemplified this conclusion by its use of observations from Zadko and VIRT. The locations of these two telescopes, in Western Australia and the Caribbean, respectively, place them as rough antipodes of each other, i.e., one is at night while the other is at day, where coordinated observations allow for complete coverage of any source visible in the nocturnal sky. Fortunately, both followed GRB 170202A until its optical emission completely faded, as it was this extended sampling that uncovered the late optical flare in its afterglow.

An attempt to reproduce our analysis without knowledge of the late GRB 170202A optical flare was carried out. The resultant optical decay index was incompatible with either the X-ray data or the standard fireball model. We found this result interesting, particularly as it is the common approach of literature to dismiss such discrepancies as being explained by late flaring activity, which in turn leads to an inability to derive all the parameters of the fireball model. A main takeaway of our study, then, is that it highlights the utility of erring on the side of caution when attempting to explain discrepancies to the fireball model while relying on a light curve with *scarce* sampling.

Table 6
Parameters of the GRB 170202A Fireball Model Derived from Observations Used in this Study

Parameter	Hypothesis Value	Model Value	Hypothesis Value	Model Value
Radiative efficiency (%)	30	⋯	30	⋯
E_0 (ergs)	⋯	56.7×10^{52}	⋯	145×10^{52}
n_0	1.0	⋯	0.1	⋯
p	⋯	2.05	⋯	2.2
ϵ_e forward shock	⋯	0.02	⋯	0.01
ϵ_B forward shock	⋯	1.8×10^{-5}	⋯	0.008
Θ_j (°)	⋯	7.5	⋯	2.1
Γ	⋯	>300	⋯	125

Note. The values of GRB 110205A have been shown for comparison purposes only in the right-hand part of the table.

Dedicated instruments like the Zwicky Transient Facility (Bellm et al. 2019) and emerging networks like the Global Rapid Advanced Network Devoted to Multi-messenger Addicts (Antier et al. 2020) have been specifically designed for detecting transient events. The size of the field of view (or equivalent field of view, in the case of a network of telescopes) and the observation methods employed by these groups limit their usefulness to studies such as that undertaken for GRB 170202A here. Specifically, their observational protocols are not tuned to provide well-sampled (near-continuous) coverage of the initial or final phases of optical transients. The fast reactivity of the control software used by Zadko allowed the rising component of the optical emission of GRB 170202A to be captured. It was the scientific trade-off between the size of the field of view of Zadko and VIRT versus the rate of potential new interesting events that encouraged their continual observations of this burst until it completely faded, while simultaneously ignoring any new transient detections. It is not an intention of our study to downplay the importance of instruments and collaborations dedicated to detecting the most transient sources at any give time. We only wish to highlight how our work has shown that an equivalent importance exists for extended and coordinated observing campaigns of individual transient events, from their detection to complete fading. This conclusion should encourage other telescope teams to increase the observational time they dedicate to the optical counterparts of transient events to aid the scientific community in developing a more complete picture of the nature of GRBs. Moreover, to facilitate such future efforts, we would also encourage detection teams to consider providing a unique flag that indicates a "burst of interest" for extended follow-up, possibly based off promising results from their initial properties.

We would like to thank the anonymous referee for a very dedicated report and checks of this work. We gratefully acknowledge support through NASA-EPSCoR grant NNX13AD28A. B.G. and N.B.O. also acknowledge financial support from NASA-MIRO grant NNX15AP95A, and NASA-RID grant NNX16AL44A. P.G. and N.B.O. acknowledge financial support from NSF-EiR grant 1901296. E.M. acknowledges support support from the Zadko Undergrad Fellowship. Parts of this research were conducted by the Australian Research Council Centre of Excellence for Gravitational Wave Discovery (OzGrav), through project number CE170100004. This research has been partly conducted under the auspices of the FIGARONet collaborative network supported by the Agence Nationale de la Recherche, program ANR-14-CE33. We also dedicate this work to the late Jim Zadko, whose donation of the Zadko Telescope to the University of Western Australia and continuous support of this facility made this study possible.

ORCID iDs

B. Gendre https://orcid.org/0000-0002-9077-2025
N. B. Orange https://orcid.org/0000-0002-7198-3476
D. M. Coward https://orcid.org/0000-0002-7795-9354

References

Akerlof, C., Balsano, R., Barthelmy, S., et al. 2000, ApJL, 532, L25
Amati, L. 2006, MNRAS, 372, 233
Antier, S., Agayeva, S., Almualla, M., et al. 2020, MNRAS, 497, 5518
Barthelmy, S. D., Barbier, L. M., Cummings, J. R., et al. 2005, SSRv, 120, 14
Barthelmy, S. D., Cummings, J. R., Gehrels, N., et al. 2017, GCN, 20596, 1
Bellm, E. C., Kulkarni, S. R., Graham, M. J., et al. 2019, PASP, 131, a18002
Coward, D. M., Todd, M., Vaalsta, T. P., et al. 2010, PASA, 27, 331
Coward, D. M., Gendre, B., Tanga, P., et al. 2017, PASA, 34, e005
D'Avanzo, P., D'Elia, V., Burrows, D. N., et al. 2017, GCN, 20592, 1
de Ugarte Postigo, A., Izzo, L., Thoene, C., et al. 2017, GCN, 20584, 1
Fong, W., Berger, E., Margutti, R., et al. 2015, ApJ, 815, 102
Frail, D. A., Kulkarni, S. R., Sari, R., et al. 2001, ApJL, 562, L55
Frederiks, D., Golenetskii, S., Aptekar, R., et al. 2017, GCN, 20604, 1
Gao, H., Lei, W.-H., Zou, Y.-C., et al. 2013, NewAR, 57, 141
Gao, H., Wang, X.-G., Mészáros, P., et al. 2015, ApJ, 810, 160
Gehrels, N., Chincarini, G., Giommi, P., et al. 2004, ApJ, 611, 1005
Gendre, B., Attela, J. L., Boër, M., et al. 2012, ApJ, 748, 59
Gendre, B., Corsi, A., Cutini, S., et al. 2009, in AIP Conf. Proc. 1133 (Melville, NY: AIP), 175
Gendre, B., Galli, A., Corsi, A., et al. 2007, A&A, 462, 565
Gendre, B., Orange, N. B., Morris, D. C., et al. 2019, RMxAC, 51, 9, RMxAC..51
Gendre, B., Orange, N., Morris, D., et al. 2017, GCN, 20598, 1
Giblin, T. W., Neff, J. E., Hakkila, J., David, K., & Hartmann, D. 2004, AN, 325, 670
Guidorzi, C., Kobayashi, S., Steele, I. A., Gomboc, A., & Mundell, C. G. 2017a, GCN, 20579, 1
Guidorzi, C., Kobayashi, S., Steele, I. A., Gomboc, A., & Mundell, C. G. 2017b, GCN, 20593, 1
Im, M., Kim, Y., Kim, J., & Struve, O. 2017a, GCN, 20594, 1
Im, M., Kim, Y., Kim, J., & The, T. 2017b, GCN, 20601, 1
Klebesadel, R., Strong, I., & Olson, R. 1973, ApJL, 182, L85
Klotz, A., Boër, M., Atteia, J. L., & Gendre, B. 2009a, AJ, 137, 4100
Klotz, A., Gendre, B., Atteia, J. L., et al. 2009b, ApJL, 697, L18
Klotz, A., Gendre, B., Stratta, G., et al. 2006, A&A, 451, L39
Klotz, A., Turpin, D., MacPherson, D., et al. 2017a, GCN, 20599, 1
Klotz, A., Turpin, D., MacPherson, D., et al. 2017b, GCN, 20580, 1
Kruehler, T., de Ugarte Postigo, A., & Hakala, P. J. 2017, GCN, 20582, 1
Krühler, T., Greiner, J., McBreen, S., et al. 2009, ApJ, 697, 758
Kuin, N. P. M., & Racusin, J. L. 2017, GCN, 20587, 1
Kumar, P. 2000, ApJL, 538, L125
Kumar, P., & Panaitescu, A. 2000, ApJL, 541, L51
Kumar, P., & Zhang, B. 2015, PhR, 561, 1
Lazzati, D., Rossi, E., Covino, S., et al. 2002, A&A, 396, L5

Mészáros, P., & Rees, M. J. 1997, ApJ, 476, 232
Metzger, M. R., Djorgovski, S. G., Kulkarni, S. R., et al. 1997, Natur, 387, 878
Mooley, K. P., Staley, T. D., Fender, R. P., et al. 2017, GCN, 20666, 1
Mori, H., Nakaoka, T., Kawabata, M., et al. 2017, GCN, 20581, 1
Morris, D. C., Gendre, B., Orange, N. B., et al. 2018, AAS, 231, 442.07
Neff, J. E., Allen, D. K., Aurin, D. M., et al. 2004, AN, 325, 669
Orange, N. B., Morris, D., Gokuldass, P., Lombardi, T., & Parsons, M. 2021, AAS, 53, 139.02
Osborne, J. P., Beardmore, A. P., Evans, P. A., & Goad, M. R. 2017, GCN, 20586, 1
Panaitescu, A., & Kumar, P. 2000, ApJ, 543, 66
Panaitescu, A., Mészáros, P., & Rees, M. J. 1998, ApJ, 503, 314
Racusin, J. L., Barthelmy, S. D., Cenko, S. B., et al. 2017, GCN, 20575, 1
Rees, M. J., & Mészáros, P. 1992, MNRAS, 258, 41
Romano, P., Campana, S., Chincarini, G., et al. 2006, A&A, 456, 917
Saito, Y., Itoh, R., Tachibana, Y., et al. 2017, GCN, 20585, 1
Sari, R., Piran, T., & Halpern, J. P. 1999, ApJL, 519, L17
Schlafy, E. F., & Finkbeiner, D. P. 2011, ApJ, 737, 103
Sonbas, E., Guver, T., de Pasquale, M., et al. 2017, GCN, 20591, 1
Stratta, G., Gendre, B., Atteia, J. L., et al. 2013, ApJ, 779, 66
Vaughan, S., Goad, M. R., Beardmore, A. P., et al. 2006, ApJ, 638, 920
Vedrenne, G., & Atteia, J.-L. 2009, Gamma-Ray Bursts: The Brightest Explosions in the Universe (Berlin: Springer), 2010
Willingale, R., O'Brien, P. T., Osborne, J. P., et al. 2007, ApJ, 662, 1093
Yost, S. A., Harrison, F. A., Sari, R., & Frail, D. A. 2003, ApJ, 597, 459
Zacharias, N., Monet, D. G., Levine, S. E., et al. 2004, AAS, 205, 4815
Zhang, B. 2018, The Physics of Gamma-ray Bursts (Cambridge: Cambridge Univ. Press)
Zhang, B., Fan, Y. Z., Dyks, J., et al. 2006, ApJ, 642, 354
Zhang, B., Kobayashi, S., & Mészáros, P. 2003, ApJ, 595, 950
Zhang, B., & Yan, H. 2011, ApJ, 726, 90